Continental Shelf Research 31 (2011) 1180–1192

Contents lists available at ScienceDirect

Continental Shelf Research

journal homepage: www.elsevier.com/locate/csr

Inorganic carbon dynamics during northern California coastal upwelling

Andrea J. Fassbender [a,*], Christopher L. Sabine [b], Richard A. Feely [b], Chris Langdon [c], Calvin W. Mordy [d]

[a] School of Oceanography, University of Washington, 1503 NE Boat Street, mailbox #355351, Seattle, WA 98195-4340, USA
[b] Pacific Marine Environmental Laboratory/National Oceanic and Atmospheric Administration, 7600 Sand Point Way NE, Seattle, WA 98115-6349, USA
[c] Rosenstiel School of Marine and Atmospheric Science, University of Miami, 4600 Rickenbacker Causeway, Miami, FL 33149-2507, USA
[d] Joint Institute for the Study of the Atmosphere and Ocean, Box 355672, University of Washington, Seattle, WA 98105-5672, USA

ARTICLE INFO

Article history:
Received 17 May 2010
Received in revised form
14 March 2011
Accepted 19 April 2011
Available online 3 May 2011

Keywords:
Carbon
Upwelling
Acidification
California
Continental shelf
Phytoplankton

ABSTRACT

Coastal upwelling events in the California Current System can transport subsurface waters with high levels of carbon dioxide (CO_2) to the sea surface near shore. As these waters age and are advected offshore, CO_2 levels decrease dramatically, falling well below the atmospheric concentration beyond the continental shelf break. In May 2007 we observed an upwelling event off the coast of northern California. During the upwelling event subsurface respiration along the upwelling path added $\sim$35 μmol kg^{-1} of dissolved inorganic carbon (DIC) to the water as it transited toward shore causing the waters to become undersaturated with respect to Aragonite. Within the mixed layer, pCO_2 levels were reduced by the biological uptake of DIC (up to 70%), gas exchange (up to 44%), and the addition of total alkalinity through $CaCO_3$ dissolution in the undersaturated waters (up to 23%). The percentage contribution of each of these processes was dependent on distance from shore. At the time of measurement, a phytoplankton bloom was just beginning to develop over the continental shelf. A box model was used to project the evolution of the water chemistry as the bloom developed. The biological utilization of available nitrate resulted in a DIC decrease of $\sim$200 μmol kg^{-1}, sea surface pCO_2 near $\sim$200 ppm, and an aragonite saturation state of $\sim$3. These results suggest that respiration processes along the upwelling path generally increase the acidification of the waters that are being upwelled, but once the waters reach the surface biological productivity and gas exchange reduce that acidification over time.

1. Introduction

Seasonal upwelling in the California Current System (CCS) brings dense water with high partial pressures of carbon dioxide ($pCO_2 > 600$ ppm) to the sea surface and into contact with the atmosphere near shore (Hales et al., 2005a; van Geen et al., 2000; Feely et al., 2008). The large gradient in pCO_2 ($\Delta pCO_2 > 200$ ppm) between the upwelled waters and the atmosphere results in the exchange of CO_2 across the air–sea interface causing these near shore upwelling regions to be local sources of CO_2 to the atmosphere (Hales et al., 2005b). As upwelled waters age and are advected offshore sea surface pCO_2 drops dramatically, reaching levels significantly lower than the atmospheric concentration seaward of the shelf break (Hales et al., 2005b; van Geen et al., 2000; Feely et al., 2008). Hence, this water transitions from a near shore regional source to an offshore regional sink for atmospheric CO_2. Processes that may be important in this transition and influence the carbon characteristics of upwelled water include biological productivity/respiration, calcium carbonate dissolution/precipitation, and air–sea gas exchange. Here we use observations from an upwelling event off the coast of northern California in May, 2007, to determine the importance of each of these processes in transforming the carbon characteristics of the upwelled water during various stages of the upwelling process.

The California Current System (CCS) is an eastern boundary current (EBC) system that flows along the west coast of the U.S. and southern Canada (Hickey, 1979; Hickey and Banas, 2008). Throughout the spring and summer seasons the mean winds are directed equatorward along the coast resulting in offshore Ekman transport at the coastline (Allen et al., 1995; Huyer et al., 1979; Huyer, 1983; Lentz, 1992; Strub et al., 1987a, b). To compensate for the offshore surface flow, nutrient and carbon rich, subsurface, coastal water is upwelled onto the continental shelf. During periods of strong equatorward wind stress this subsurface water can be upwelled into the euphotic zone (upwelling events) providing the nutrients necessary to stimulate phytoplankton blooms (MacIsaac et al., 1985).

The primary productivity that is stimulated by seasonal upwelling in EBC systems is what makes these regions some of the most productive areas in the world's ocean, accounting for

* Corresponding author. Tel.: +1 206 526 6208; fax: +1 206 526 6744.
E-mail addresses: Andrea.Fassbender@noaa.gov (A.J. Fassbender), Chris.Sabine@noaa.gov (C.L. Sabine), Richard.A.Feely@noaa.gov (R.A. Feely), CLangdon@rsmas.miami.edu (C. Langdon), Calvin.W.Mordy@noaa.gov (C.W. Mordy).

0278-4343/$ - see front matter © 2011 Elsevier Ltd. All rights reserved.
doi:10.1016/j.csr.2011.04.006

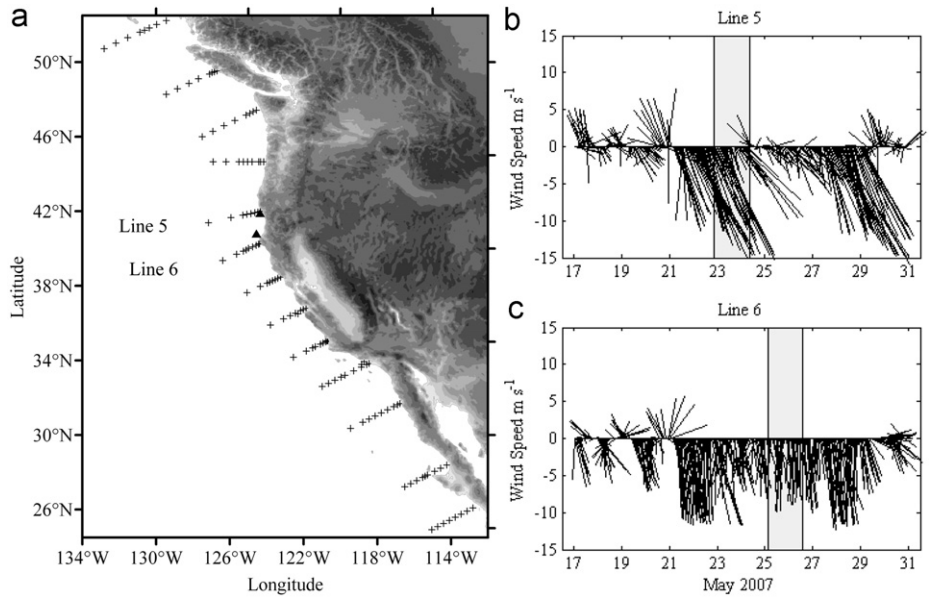

Fig. 1. (a) The *NACP West Coast Cruise* study region with plus signs representing station locations. The two triangles near shore, by Lines 5 and 6, indicate the locations of the National Data Buoy Center (NDBC) (http://www.ndbc.noaa.gov/) buoys where wind data were collected. (b) 10 m wind speeds from NDBC buoy #46027 near Line 5 and (c) from NDBC buoy #46022 near Line 6 are shown. Negative (positive) wind speeds indicate upwelling (downwelling) favorable conditions. The shaded region in each figure indicates when the line was occupied during the cruise.

~10–15% of the global ocean new production (Chavez and Toggweiler, 1995). In most EBC systems, the nutrients that fuel primary productivity during upwelling events are generally the byproducts of organic matter decomposition. In the CCS, ~1/3 of the upwelled nutrients are preformed; these are the nutrients that were present when the water was last at the sea surface (Hales et al., 2005b). These preformed nutrients are what allow phytoplankton to reduce sea surface pCO_2 to levels significantly below atmospheric concentrations in the CCS (Hales et al., 2005b; van Geen et al., 2000).

In addition to nutrients, primary producers are sensitive to the carbon characteristics of upwelled waters, yet few studies in the CCS have included rigorous carbonate chemistry analysis (Hales et al., 2005b; Ianson et al., 2003). In the May and the June of 2007 the *North American Carbon Program West Coast Cruise* was conducted to document the carbon and nutrient characteristics of coastal water along the continental shelf of western North America during the upwelling season. Thirteen cross-shelf transects between Queen Charlotte Sound, Canada, and San Gregorio Baja California Sur, Mexico, were sampled for water mass characteristics (Fig. 1a). During the cruise an upwelling event off the coast of northern California brought waters undersaturated with respect to aragonite to the sea surface (Feely et al., 2008). Here we evaluate how biological productivity/respiration, calcium carbonate dissolution/precipitation, and gas exchange were influencing the carbon characteristics of these waters as they were transported toward shore, upwelling into the mixed layer, and advected offshore over time.

2. Measurements and methods

At each station, conductivity, temperature, and pressure measurements were made over the full water column and discrete water samples were collected from 12-l Niskin-type bottles for dissolved inorganic carbon (DIC), Total Alkalinity (TA), oxygen, and nutrient analysis. DIC was analyzed by gas extraction and coulometry using a modified Single-Operator Multi-Metabolic Analyzer (SOMMA) system with a precision of ± 1.5 μmol kg^{-1} (Johnson et al., 1985, 1987, 1993; Johnson, 1992; Wilke et al., 1993). Seawater TA was measured using the method of acidimetric titration described by Dickson et al. (2003), at a precision of ± 2 μmol kg^{-1}. Oxygen concentrations were determined with a precision of ± 0.2 μmol kg^{-1} using the whole-bottle titration technique of Carpenter (1965) with modifications by Culberson and Knapp (1991). Titrations were completed using an MBARI-designed automated oxygen titrator and the MBARI oxygen program written by Gernot Friedrich (MBARI). Nutrient samples were analyzed with a continuous flow analyzer using the WOCE hydrographic program protocols (Gordon et al., 1992) at a precision of 0.2 μmol kg^{-1} for nitrate, 0.03 μmol kg^{-1} for phosphate, and 0.2 μmol kg^{-1} for silicic acid.

3. Calculations

3.1. Mixed layer depth criterion

To define a mixed layer depth criterion that could be used at each station in the northern California region various ranges in potential density difference ($\Delta\sigma_\theta$) between the sea surface and the underlying water were evaluated. For each $\Delta\sigma_\theta$ criterion the standard deviation of the resulting mixed layer depths was compared to the mean mixed layer depth. Any $\Delta\sigma_\theta$ criterion resulting in a standard deviation value that was less than the mean mixed layer depth was considered appropriate (Lentz, 1992). From the range of appropriate $\Delta\sigma_\theta$ criteria that were determined, 0.035 had the smallest standard deviation and is used here.

3.2. Carbon transformations during water transit

In order to isolate changes in DIC mediated from biological processes, on each transect, we determined the change in concentration of non-conservative properties (NO_3^- and TA) along density surfaces relative to an offshore source or reference station (e.g. $\Delta NO_3^- = NO_{3\text{station}}^- - NO_{3\text{source}}^-$). Before making these calculations, the DIC, NO_3^-, and TA data were salinity normalized to the

mean salinity in the upper 350 m to account for minor changes in salinity that occur along the density surface as it upwells and warms. At each station, data were linearly interpolated onto $0.1\sigma_\theta$ levels so that changes along density surfaces could be evaluated. In order to use changes in non-conservative properties as proxies for biological processes, conservative water mass characteristics must not be changing along density surfaces. The introduction of a new water mass along the upwelling path could easily be misinterpreted as a chemical process. *T–S* plots were used to determine if water inshore of the selected source station was the same on the density surfaces outcropping over the continental shelf.

The production of organic biomass and oxygen during photosynthesis requires the assimilation of CO_2 and nutrients at specific, well known ratios (Redfield et al., 1963). A more recent evaluation of these ratios by Anderson and Sarmiento (1994) is used here:

$$HPO_4^{2-} + 16NO_3^- + 117CO_2 + 170H_2O + 18H^+ \leftrightarrow C_{117}H_{359}O_{286}N_{16}P_1 + 170O_2 \quad (1)$$

The uptake of CO_2 and nutrients during photosynthesis influences the concentration of TA (Eq. (2)) and DIC (Eq. (3)). The biological uptake of 16 μmol kg^{-1} NO_3^- and 1 μmol kg^{-1} HPO_4^{2-} from seawater also requires the uptake of 18 μmol kg^{-1} H^+ for charge neutrality, increasing the TA by 18 μmol kg^{-1} (Eq. (1)). However, the uptake of 1 μmol kg^{-1} HPO_4^{2-} reduces TA resulting in a decrease of 1 μmol kg^{-1} in TA. The net influence of biological productivity on TA is an increase of 17 μmol kg^{-1} for every 16 μmol kg^{-1} NO_3^- assimilated ($R_{(TA/NO_3)} = -17:16$). Accompanying the assimilation of 16 μmol kg^{-1} NO_3^- is the uptake of 117 μmol kg^{-1} CO_2, giving a stoichiometric DIC:NO_3^- assimilation ratio of $R_{(DIC/NO_3)} = 117:16$. This process also results in the production of 170 μmol kg^{-1} of O_2 giving a stoichiometric O_2:NO_3^- assimilation ratio of $R_{(O_2/NO_3)} = -170:16$:

$$TA = [HCO_3^-] + 2[CO_3^{2-}] + [B(OH)_4^-] + [HPO_4^{2-}] + 2[PO_4^{3-}] + \cdots + [OH^-] - [H^+] \quad (2)$$

$$DIC = [CO_2] + [H_2CO_3] + [HCO_3^-] + [CO_3^{2-}] \quad (3)$$

The stoichiometric relationships between DIC, TA, and NO_3^- during photosynthesis, as well as the reverse process of respiration, made it possible to use changes in the concentration of nitrate (ΔNO_3^-) to infer changes in DIC (Eq. (4)) and TA (Eq. (5)) driven by organic matter (O.M.) production/respiration:

$$\Delta DIC_{O.M.} = R_{(DIC/NO_3)}\,\Delta NO_3^- \quad (4)$$

$$\Delta TA_{O.M.} = R_{(TA/NO_3)}\,\Delta NO_3^- \quad (5)$$

Calcium carbonate ($CaCO_3$) precipitation and dissolution (Eq. (6)) also have an influence on the DIC and TA of seawater, and changes in DIC caused by these processes can be estimated using ΔTA. The uptake of 1 μmol kg^{-1} CO_3^{2-} during calcification results in a 2 μmol kg^{-1} decrease in TA and a 1 μmol kg^{-1} decrease in DIC. After subtracting $\Delta TA_{O.M.}$ from the measured ΔTA (Eq. (7)) the remaining changes in TA along the density surface (ΔTA_{CaCO_3}) were used to determine the influence of calcium carbonate precipitation/dissolution on DIC (Eq. (8)):

$$Ca^{2+} + CO_3^{2-} \leftrightarrow CaCO_{3(s)} \quad (6)$$

$$\Delta TA_{CaCO_3} = \Delta TA - \Delta TA_{O.M.} \quad (7)$$

$$\Delta DIC_{CaCO_3} = 0.5 \times \Delta TA_{CaCO_3} \quad (8)$$

After accounting for the biologically driven changes in DIC ($\Delta DIC_{O.M.}$ and ΔDIC_{CaCO_3}), we subtracted them from the measured DIC changes ($\Delta DIC = DIC_{station} - DIC_{source}$). This left a residual component reflecting all of the processes that were not considered in this analysis (Eq. (9)). The uncertainty in these calculations is discussed in the Appendix:

$$\Delta DIC_{residual} = \Delta DIC - \Delta DICO_{O.M.} - \Delta DIC_{CaCO_3} \quad (9)$$

3.3. Carbon transformations in the mixed layer

The photosynthetic uptake of CO_2 during phytoplankton blooms can have a dramatic influence on sea surface DIC during upwelling events in the CCS (Hales et al., 2005b; van Geen et al., 2000). To evaluate the magnitude of this influence we compared NO_3^-, TA, and DIC samples from the mixed layers of stations sampled over the continental shelf on Lines 5 and 6 (Fig. 1a) to samples taken from a reference depth below the mixed layer. The reference depth for a given station was selected as the nearest seaward, neighboring station with a sample on the same density surface. Due to the upward tilt of isopycnals near-shore and the coarse across-shelf sampling, reference depths were generally deeper than the mixed layer depths. Concentration differences between the reference sample and the mixed layer sample reflect the net changes that occurred from the time the water left the reference location until the time of measurement. This means that the net community production estimated below will include a component of respiration below the mixed layer, but this contribution is very small compared to the mixed layer changes.

In the mixed layer, gas exchange and net biological productivity influence the oxygen content of the water. The change in oxygen (ΔO_2) between the reference depth and the mixed layer therefore reflects how much oxygen has been gained by these processes and can be used to determine how long the water has been in the mixed layer. Using a box model approach, the change in oxygen over time is equal to the sources of oxygen minus the sinks:

$$h(\Delta O_2/\Delta t) = B\,R_{(O_2/NO_3)} + F \quad (10)$$

$$B = h(\Delta NO_3^-/\Delta t) \quad (11)$$

where h is the mixed layer depth, Δt is the mixed layer age, B is the net community production (NCP) rate term and F is the gas exchange term. The NCP rate term is derived from ΔNO_3^-, the mixed layer depth and the mixed layer age (Eq. (11)). This gives two equations and two unknowns (B and Δt). Biological productivity and gas exchange influence the oxygen concentration of the mixed layer simultaneously; however, the simple box model (Eq. (10)) requires these processes to be considered independently in order to solve for Δt. Combining Eqs. (10) and (11) and using a fixed time step we created a more sophisticated model that works backward in time, incrementally calculating the oxygen gained from gas exchange and biological productivity during each time step:

$$\Delta O_{2(t=n)} = (B_{initial}\,R_{(O_2/NO_3)} + F_{(t=n)})t/h \quad (12)$$

$$F_{(t=n)} = k_{(t=n)}([O_2]_{h(t=n)} - [O_2]_{sat}) \quad (13)$$

$$[O_2]_{h(t=n+1)} = [O_2]_{h(t=n)} - \Delta O_{2(t=n)} \quad (14)$$

where k is the gas transfer velocity, $[O_2]_h$ is the oxygen concentration in the mixed layer, $[O_2]_{sat}$ is the oxygen saturation concentration and $(t=n+1)$ is the next model iteration going backward in time. For each time step the gas exchange term is calculated (Eq. (13)) and used in Eq. (12) to determine how much oxygen the mixed layer gained during that time step. The oxygen gain (ΔO_2) is then used to update the mixed layer oxygen concentration for the next time step (Eq. (14)). Over time the

mixed layer oxygen concentration is reduced to what it was when the water initially upwelled into mixed layer from the reference depth. The number of time steps necessary to reach this point is then used to determine the age of the mixed layer. When the mixed layer age (Δt) is determined, if $B_{initial}$ is not equal to B, then $B_{initial}$ is adjusted and the model is re-run until there is a match. Using this iterative method we were able to solve for Δt and B.

Model input parameters include an initial, fixed biological productivity term ($B_{initial} \propto 1\ g\ C\ m^{-1}\ d^{-1}$), chosen based on literature values from the region (Chavez et al., 1991; Dugdale et al., 2006; Pilskaln et al., 1996), 10 min National Data Buoy Center (NDBC) winds (http://www.ndbc.noaa.gov/) converted from 5 to 10 m using the factor applied by Jiang et al. (2008), a fixed O_2 Schmidt number, and a fixed mixed layer saturation concentration of oxygen ($[O_2]_{sat}$). The O_2 Schmidt number (kinematic viscosity/diffusion coefficient) is calculated from the laboratory determined diffusion coefficients of Wise and Houghton (1966) and kinematic viscosity. The mixed layer saturation concentration of oxygen ($[O_2]_{sat}$) is calculated using the temperature and salinity fit of Garcia and Gordon (1992). Gas transfer velocities (k) are calculated from the 10 min winds and the Schmidt number using the relationship of Nightingale et al. (2000) and are used to determine the gas exchange term (F) during each time step (13). The quadratic parameterization of gas transfer velocity with the wind speed of Nightingale et al. (2000) has been corroborated in recent studies on air–sea gas exchange (Wanninkhof et al., 2009; Sweeney et al., 2007), providing support for our choice to use this parameterization.

Once the mixed layer age is determined the net exchange of CO_2 between the sea surface and the atmosphere over this time period is calculated in a similar model. Input parameters for this model include a CO_2 solubility constant calculated from the laboratory temperature and salinity fit of Weiss (1974), the same 10 min NDBC winds (http://www.ndbc.noaa.gov/) used in the oxygen model, and a fixed CO_2 Schmidt number calculated using the temperature relationship of Wanninkhof (1992) based on diffusion coefficients determined experimentally by Jahne et al. (1987). At the start of each 10 min time step the CO_2 gas exchange term (F) is calculated (Eq. (15)) using the Nightingale et al. (2000) parameterization with 10 min buoy winds and the CO_2 Schmidt number. The CO_2 flux is then converted into a concentration of DIC lost due to gas exchange (ΔDIC_{Gas}). The ΔDIC_{Gas}, $\Delta DIC_{O.M.}$, and ΔDIC_{CaCO_3} for that time step are then subtracted from DIC_h to update the mixed layer DIC concentration for the next time step (Eq. (16)). The TA_h is also updated for changes resulting from net biological productivity and $CaCO_3$ dissolution (Eq. (17)):

$$F_{(t=n)} = k_{(t=n)}\, C(pCO_{2(t=n)} - pCO_{2(atm)}) \quad (15)$$

$$DIC_{h(t=n+1)} = DIC_{h(t=n)} - \Delta DIC_{O.M.(t=n)} - \Delta DIC_{Gas(t=n)} - \Delta DIC_{CaCO_3(t=n)} \quad (16)$$

$$TA_{h(t=n+1)} = TA_{h(t=n)} - \Delta TA_{O.M.(t=n)} - \Delta TA_{CaCO_3(t=n)} \quad (17)$$

where k is the gas transfer velocity, C is the CO_2 solubility constant (Weiss, 1974), and $pCO_{2(atm)}$ is the atmospheric partial pressure of CO_2 from the Carbon Dioxide Information Analysis Center (CDIAC). The updated TA_h and DIC_h are used in the CDIAC pCO_2 program of Lewis and Wallace (1998) with equilibrium constants from Mehrbach et al. (1973) as re-fit by Dickson and Millero (1987) to re-equilibrate the carbonate system and determine the equilibrium pCO_2 for the flux calculation in the next time step. This process is repeated over the age of mixed layer and at the end of this process ΔDIC_{Gas} terms are summed to yield the total loss of DIC to the atmosphere by gas exchange. Uncertainty in the model output is discussed in the Appendix.

4. Results

4.1. Carbon transformations during water transit

During the cruise, two of the thirteen cross-shelf transects (Lines 5 and 6) were conducted off the coast of northern California where an upwelling event was occurring (Fig. 1a). Two days prior to sampling on Line 5, the winds reversed from a ~4-day relaxation period to upwelling favorable conditions and initiated an upwelling event (Fig. 1b). By the time Line 6 was sampled the winds had been upwelling favorable for ~4 days (Fig. 1c) and had weakened relative to the winds observed at the beginning of the reversal. On both transects upwelled water was outcropping near shore over the continental shelf (Fig. 2a and b). On Line 5, the surface concentrations of DIC (~2175 μmol kg^{-1}), pCO_2 (~1000 ppm), and nitrate (~30 μmol kg^{-1}) over the continental shelf were high and decreased rapidly moving offshore. On Line 6, the surface concentrations of DIC (~2135 μmol kg^{-1}), pCO_2 (~775 ppm), and nitrate (~25 μmol kg^{-1}) over the continental shelf were notably lower but increased seaward of the slope before decreasing rapidly offshore. Beyond ~60 km from shore surface waters on both transects were nearly devoid of nitrate and undersaturated with respect to pCO_2.

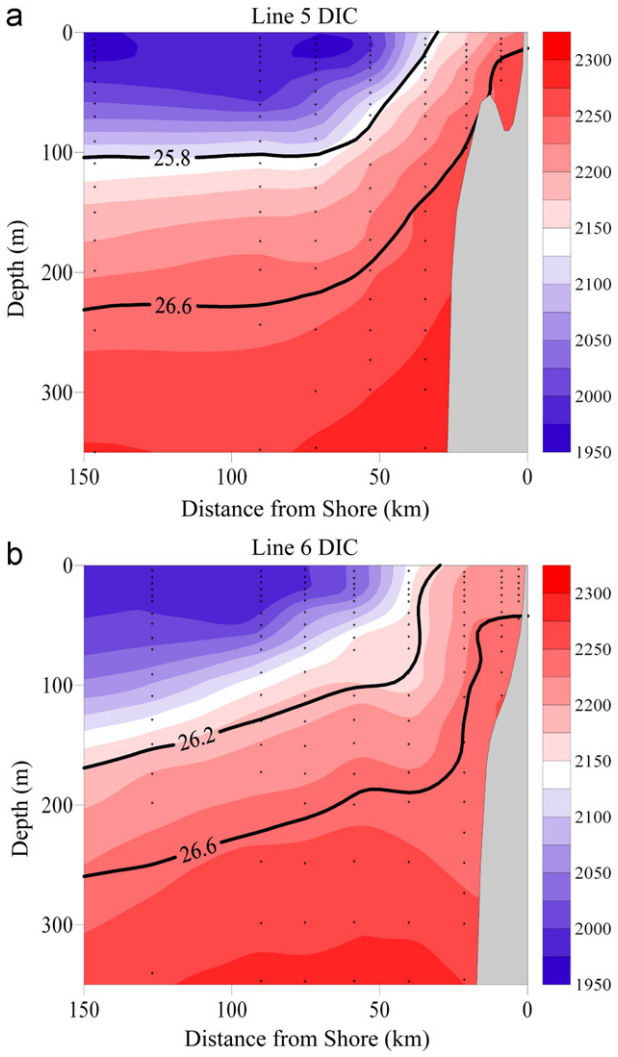

Fig. 2. Section plots of DIC for (a) Line 5 and (b) Line 6 contoured at 25 μmol kg^{-1}. Black dots indicate the depths where samples were taken at each station and thick black lines represent two of the σ_θ surfaces that were outcropping over the continental shelf and slope region at the time of sampling.

Density surfaces upwelling over the continental shelf in this region originated from between 125 and 350 m depth offshore (Fig. 2a and b). The conservative and non-conservative water mass characteristics of offshore water within this depth range were homogeneous over a broad spatial scale ranging from the coast of Washington to central California. As a result, waters upwelling at the coastline throughout the study region originated from the same offshore water mass and initially had the same property concentrations. Acoustic Doppler Current Profiler (ADCP) data between 350 m and the surface indicate that north south flow velocities in this region were generally $\sim$0.1 m s^{-1}, suggesting localized advection. The along shore advection of coastal waters causes signals resulting from biological and physical processes in one location to be transported to other locations within the region. As a result, the near shore observations made on each transect largely reflect a regionally integrated (up to $\sim$30 km) signal rather than immediately local processes. Regions of higher north south current velocities (0.5 m s^{-1}) were restricted to the shelf and slope region where transient currents as well as the seasonal equatorward jet and undercurrent generally reside (Hickey, 1979, 1998). Even with more rapid currents near shore there was not enough time for water on one line to be transported to an adjacent line by the time sampling occurred, which prevented the ship from tracking the same patch of water over time.

The cross-shelf spatial patterns of ΔDIC (Fig. 3a and b) and ΔNO_3^- were very similar to each other on each transect and ΔNO_3^-

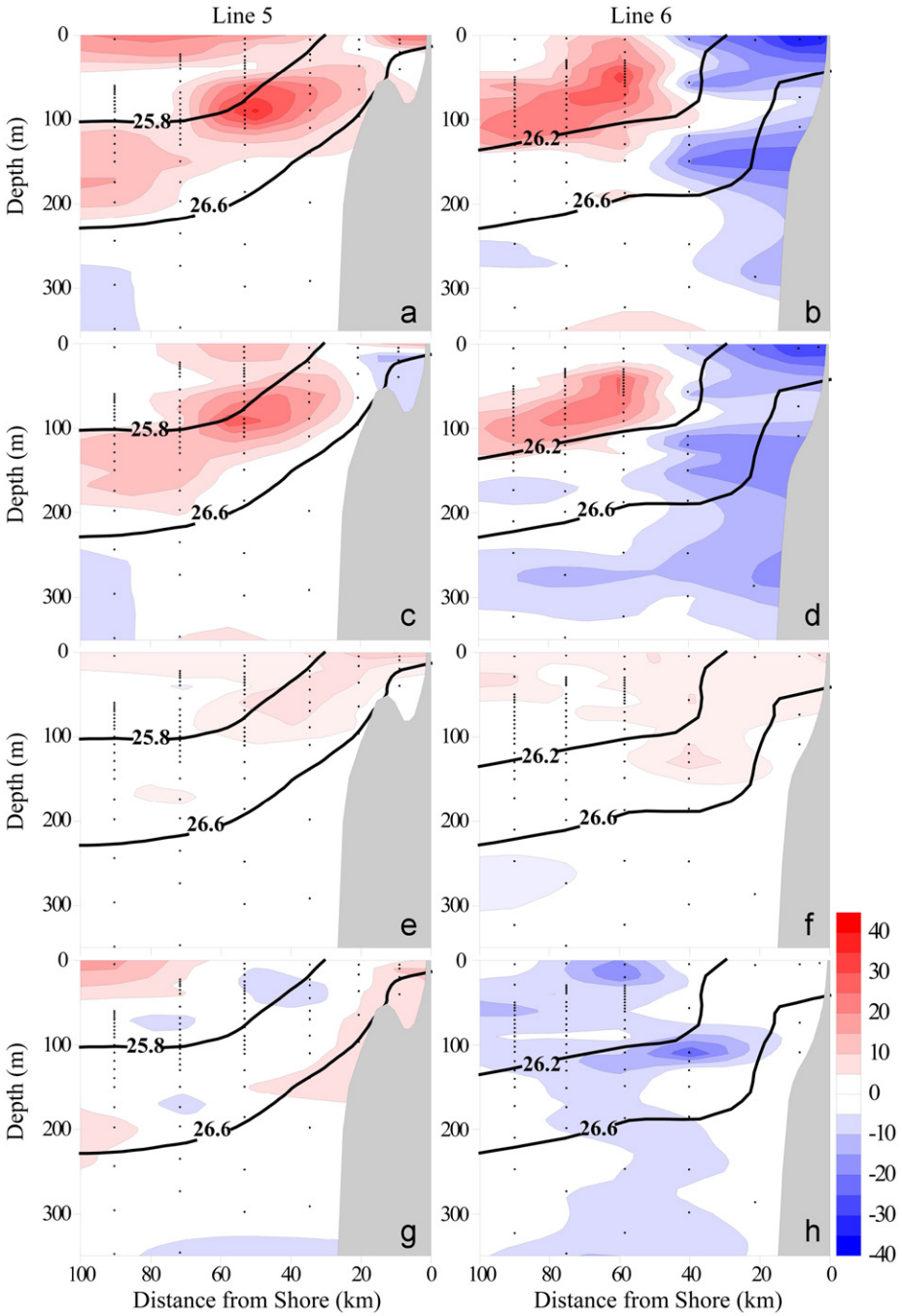

Fig. 3. (a, b) ΔDIC, (c, d) $\Delta DIC_{O.M.}$, (e, f) ΔDIC_{CaCO_3}, and (g, h) $\Delta DIC_{residual}$ for Lines 5 and 6 contoured at $\pm$5 μmol kg^{-1}. Black dots indicate the depths of σ_θ surfaces that the data were interpolated onto and thick black lines represent two of the σ_θ surfaces that were outcropping over the continental shelf and slope region at the time of sampling.

was used to estimate the organic matter production/respiration component (Eq. (4)) of the total DIC changes. This resulted in spatial patterns of $\Delta DIC_{O.M.}$ (Fig. 3c and d), which were very similar to the patterns of ΔDIC, indicating that organic matter processes were responsible for a majority of the DIC changes. Regions of elevated $\Delta DIC_{O.M.}$ indicate areas where respiration was occurring in the water column, while low $\Delta DIC_{O.M.}$ values indicate regions where biological productivity was occurring. On Line 5 the waters outcropping over the continental shelf originated from the offshore respiration region where $\Delta DIC_{O.M.}$ values were high. By the time these waters reached the sea surface the $\Delta DIC_{O.M.}$ values had been greatly reduced as a result of biological productivity. On Line 6 the isopycnals influenced by respiration outcropped seaward of the shelf break and waters outcropping over the continental shelf had very low $\Delta DIC_{O.M.}$ values as a result of biological productivity.

After correcting the ΔTA for changes caused by organic matter production/respiration (Eq. (7)), the ΔTA_{CaCO_3} was converted to ΔDIC_{CaCO_3} (Eq. (8)) for each transect. On Line 5 there was a smooth gradient of increasing ΔDIC_{CaCO_3} along the upwelling path (Fig. 3e) with the highest value located near shore in surface waters over the continental shelf. On Line 6 ΔDIC_{CaCO_3} concentrations were elevated over a large region of surface and subsurface waters (Fig. 3f), extending well offshore from the continental shelf but were not as high as those observed on Line 5. After accounting for the organic matter and $CaCO_3$ process contributions to the ΔDIC, the remaining pattern (Fig. 3g and h) reflects the changes in DIC caused by other processes $\Delta DIC_{residual} = \Delta DIC - \Delta DIC_{O.M.} - \Delta DIC_{CaCO_3}$. Most of the $\Delta DIC_{residual}$ values along the isopycnals upwelling over the continental shelf were within ± 5 μmol kg^{-1} of zero, indicating that majority of the DIC transformations could be accounted for by the biological processes included in this analysis.

4.2. Carbon transformations in the mixed layer

Biological contributions to ΔDIC ($\Delta DIC_{O.M.}$ and ΔDIC_{CaCO_3}) within the mixed layer were calculated with Eqs. (4) and (8) where ΔNO_3^- and ΔTA were determined using a reference station below the mixed layer as the source water. In order to estimate the influence of gas exchange on the mixed layer ΔDIC we first had to determine how long the water had been in contact with the atmosphere at the time of measurement. To do this we used changes in the oxygen concentration of the mixed layer relative to a reference station below the mixed layer as a proxy for time evolution. This allowed us to determine mixed layer ages (Δt) and net community production (NCP) rates for the three stations over the continental shelf on each transect (Table 1). On Line 5 the mixed layer ages ranged from 0.22 to 0.7 days and increased moving away from shore. On Line 6 the mixed layer ages were larger, ranging from 3.0 to 4.1 days, and also increased moving offshore. The NCP rates on Line 5 ranged from 0.6 to 15 g C m^{-2} d^{-1}, with the highest rate at the second station from shore where a bloom was developing. On Line 6 NCP rates were lower ranging from 0.7 to 4 g C m^{-2} d^{-1}, and increased moving away from shore.

The NCP rates and the mixed layer ages were then used in a similar model to determine the total amount of DIC lost from each mixed layer by gas exchange (ΔDIC_{Gas}). Subtracting the organic matter, $CaCO_3$, and gas exchange components from the measured ΔDIC left a residual component ($\Delta DIC_{residual}$) representing the mixed layer DIC changes caused by processes that were not considered here (Table 2). On both transects biological productivity was responsible for most of the DIC transformations at the mid-shelf and shelf break stations. At the near-shore stations on both lines this was not the case. On Line 5, $CaCO_3$ dissolution accounted for most of the ΔDIC at the near-shore station and on Line 6, gas exchange was the more dominant process. Gas exchange had a larger influence on the ΔDIC than biological productivity at the near-shore stations on both lines.

For each time step in the CO_2 gas exchange model TA and DIC were used to calculate sea surface pCO_2 and aragonite and calcite saturation states (Ω_{Ar}, Ω_{Ca}) using the program of Lewis and Wallace (1998) with equilibrium constants from Mehrbach et al. (1973) as re-fit by Dickson and Millero (1987). From the time the water left the reference depth until the time we measured it, the pCO_2 had decreased as a result of biological productivity, $CaCO_3$ dissolution, and gas exchange at all stations evaluated (Table 3). The reference depth samples for waters outcropping at the near-shore and mid-shelf stations on Line 5 were undersaturated with respect to aragonite ($\Omega_{Ar} < 1$). By the time we sampled the mixed layer at the mid-shelf station the water had been returned to saturated conditions but the near-shore station mixed layer was still undersaturated. On Line 6, reference depth samples for all three of the stations over the continental shelf were undersaturated with respect to aragonite. Saturation was restored at the near-shore and mid-shelf stations by the time of measurement but not at the shelf break station where the upwelled water had the lowest source water Ω_{Ar}. All stations on Lines 5 and 6 were supersaturated with respect to

Table 1
Net community production (NCP) rates and mixed layer ages (Δt).

	NCP (g C m^{-2} d^{-1})	Δt (days)
Line 5		
Near-shore	0.6 ± 0.9	0.22 ± 0.04
Mid-shelf	15 ± 5	0.36 ± 0.07
Shelf break	3 ± 1	0.7 ± 0.2
Line 6		
Near-shore	0.7 ± 0.3	3.1 ± 0.7
Mid-shelf	2.8 ± 0.9	3.0 ± 0.6
Shelf break	4 ± 1	4.1 ± 0.6

Table 2
Mixed layer depths (h) and mixed layer ΔDIC, ΔNO_3^-, ΔTA, $\Delta DIC_{O.M.}$, ΔDIC_{CaCO_3}, ΔDIC_{Gas}, and $\Delta DIC_{residual}$.

	h (m)	ΔDIC (μmol kg^{-1})	ΔNO_3^- (μmol kg^{-1})	ΔTA (μmol kg^{-1})	$\Delta DIC_{O.M.}$ (μmol kg^{-1})	ΔDIC_{CaCO_3} (μmol kg^{-1})	ΔDIC_{Gas} (μmol kg^{-1})	$\Delta DIC_{residual}$ (μmol kg^{-1})
Line 5								
Near-shore	7	12	0	10	−2	5	−3	12 ± 6
Mid-shelf	15	−19	−4	8	−29	2	−3	11 ± 7
Shelf break	12	−22	−2	4	−16	1	−4	-3 ± 6
Line 6								
Near-shore	25	−11	−1	9	−7	4	−9	1 ± 8
Mid-shelf	37	−17	−3	3	−19	0	−6	8 ± 7
Shelf break	80	−11	−2	7	−16	3	−7	9 ± 8

Table 3
pCO_2 (μatm), Ω_{Ar}, DIC (μmol kg^{-1}), TA (μmol kg^{-1}), NO_3^- (μmol kg^{-1}), and O_2 (μmol kg^{-1}) concentrations from the mixed layer at the time of measurement and from the reference station (Ref.) below the mixed layer. Reference station depths are given in parentheses.

Line 5	Near-shore Mixed layer	Near-shore Ref. (89 m)	Mid-shelf Mixed layer	Mid-shelf Ref. (60 m)	Shelf break Mixed layer	Shelf break Ref. (80 m)
pCO_2	1004	1075	699	939	656	784
ΩAr	0.8	0.8	1.2	0.9	1.2	1.0
DIC	2226	2225	2174	2204	2130	2149
TA	2263	2254	2259	2251	2223	2219
NO_3^-	30	30	24	28	20	22
O_2	139	126	198	150	218	177
Line 6	**Near-shore Mixed layer**	**Near-shore Ref. (150 m)**	**Mid-shelf Mixed layer**	**Mid-shelf Ref. (150 m)**	**Shelf break Mixed layer**	**Shelf break Ref. (185 m)**
pCO_2	738	872	735	912	875	1123
ΩAr	1.1	0.9	1.1	0.9	0.9	0.7
DIC	2202	2213	2194	2218	2221	2244
TA	2277	2268	2271	2268	2275	2268
NO_3^-	27	28	25	28	30	32
O_2	179	155	174	155	160	101

calcite at the beginning of the upwelling event, as well as at the time of measurement.

5. Discussion

5.1. Carbon transformations during water transit

Organic matter production/respiration accounted for the majority of DIC changes that occurred along density surfaces during the observed upwelling event with $CaCO_3$ dissolution, also providing a small contribution. Spatial patterns of ΔDIC_{CaCO_3} were distinct from the patterns in $\Delta DIC_{O.M.}$ on both transects, confirming that these changes were being controlled by different processes ($CaCO_3$ precipitation/dissolution and organic matter respiration/production, respectively). Even though different processes were responsible for these DIC changes, they were not entirely unrelated. On both transects organic matter respiration caused the waters to become undersaturated with respect to aragonite. This initiated the dissolution of $CaCO_3$ particles, causing an increase in TA, and therefore an increase in DIC_{CaCO_3}, along the upwelling path.

After accounting for organic matter and $CaCO_3$ contributions to the observed ΔDIC, there was a small amount of residual ΔDIC caused by processes that were not considered in this analysis. On Line 6, residual DIC along density surfaces outcropping over the continental shelf was generally within the uncertainty limits (± 5 μmol kg^{-1}); however, on Line 5 there was a distinct region of elevated residual DIC in water overlying the continual shelf (Fig. 3g). Potential sources of this excess DIC could be denitrification, selective nutrient remineralization, and cross isopycnal mixing (Hales et al., 2005a).

The removal of NO_3^- from sediment pore-waters through the process of denitrification is one mechanism that would cause a residual DIC signal. $\Delta DIC_{O.M.}$ was estimated using ΔNO_3^- and Eq. (4). But in the case of denitrification, Eq. (4) does not hold because NO_3^- has become the oxidant and therefore will not be produced or consumed with DIC at the Anderson and Sarmiento (1994) ratio $R_{(DIC/NO_3)}$. The ΔNO_3^- signal over the continental shelf suggests that ~ 1 μmol kg^{-1} NO_3^- was removed from the water, likely through the process of denitrification. Scaling this ΔNO_3^- signal to $\Delta DIC_{O.M.}$ using Eq. (4) results in the false consumption of ~ 7 μmol kg^{-1} DIC. Considering the uncertainty in these estimates, denitrification could be responsible for the entirety of the residual DIC signal on Line 5 (~ 9 μmol kg^{-1}). Another mechanism that could be contributing to the residual DIC signal on Line 5 is the preferential degradation of carbon relative to nitrogen in organic matter overlying the shelf (Wetz et al., 2008). Both the process of denitrification and selective respiration would be accompanied by a low oxygen signal as oxygen-poor waters diffused out of sediments or as oxygen was utilized during the respiration of organic matter. Scatter plots of NO_3^- vs. DIC and NO_3^- vs. O_2 at the three shelf stations on Line 5 show deviations in property–property trends for samples taken from within the residual DIC feature matching what would be expected from either of these processes (Fig. 4a and b). These findings suggest that the residual DIC overlying the continental shelf is likely due to denitrification with a small contribution potentially coming from the selective C:N respiration of organic matter.

Irreversible cross isopycnal mixing is another mechanism that could account for residual DIC within the near shore region. This mixing is caused by turbulence in the bottom boundary layer during upwelling events and can account for $\sim 25\%$ of upwelled nitrate in shallower waters (Hales et al., 2005a). The nitrate added to lighter density surfaces through this mechanism must also be accompanied by DIC. A simple mixing calculation using the data from Line 5 and 25% volume of dense water overlying the continental shelf with 75% volume of water from a lighter density surface results in a mix with an N/C ratio that is very similar to that in the individual components (~ 0.014). The resulting $\Delta NO_3^-/\Delta DIC$ on the lighter isopycnal however is an order of magnitude larger and matches the Anderson and Sarmiento (1994) ratio (16/117; 0.14). The same result is true for a 50% contribution of denser water in the mixing calculation as well as with a different set of density surfaces entirely. Consequently this type of irreversible cross isopycnal mixing may easily be misinterpreted as a biological respiration signal but does not account for $\Delta DIC_{residual}$.

5.2. Carbon transformations in the mixed layer

The NCP rates derived here are comparable to previously reported values (0.18–7.50 g C m^{-2} d^{-1}) off the coast of California during the upwelling season (Chavez et al., 1991; Dugdale et al., 2006; Franck et al., 2005; Pilskaln et al., 1996). The role of organic matter production in mixed layer ΔDIC increased moving away from shore with the highest contribution at the mid-shelf stations on both lines (Table 2). On Line 5 the ΔDIC_{CaCO_3} contribution decreased and ΔDIC_{Gas} increased slightly moving

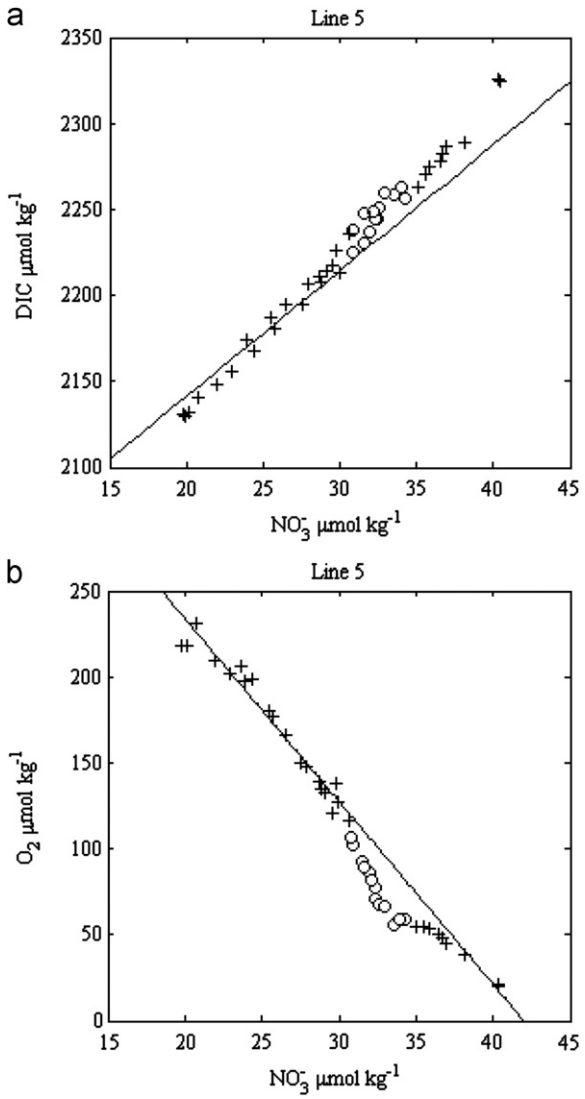

Fig. 4. (a) NO_3^- vs. DIC and (b) NO_3^- vs. O_2 using samples taken from the near-shore, mid-shelf, and shelf break stations on Line 5. Open circles indicate samples that were collected from within the $\Delta DIC_{residual}$ patch over the continental shelf. The line in each plot shows the Anderson and Sarmiento (1994) nutrient stoichiometry ($R_{(DIC/NO_3)}$=117:16; $R_{(O_2/NO_3)}$=170:16).

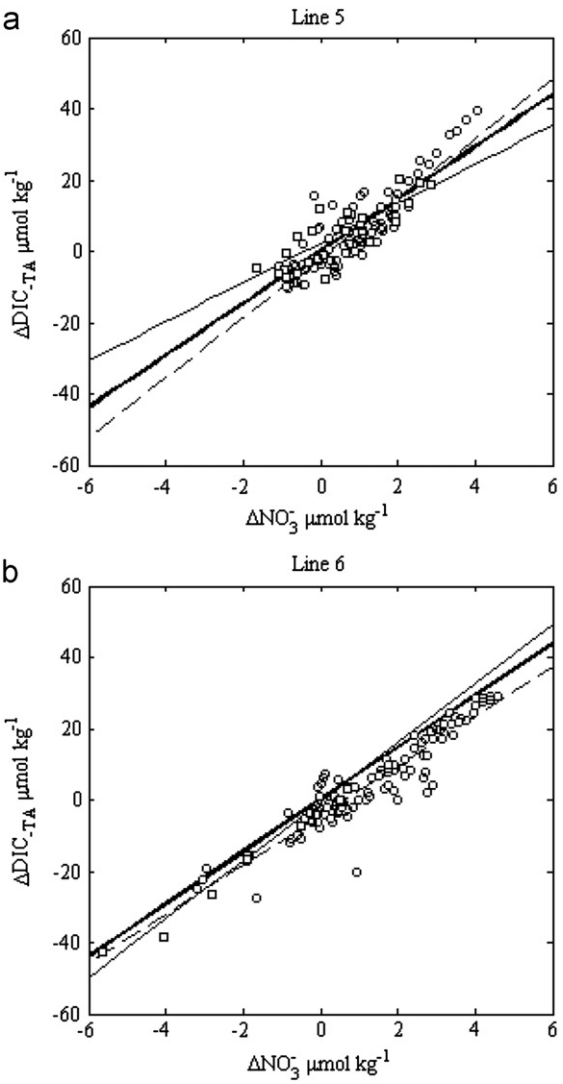

Fig. 5. ΔNO_3^- vs. ΔDIC_{-TA} for (a) Line 5 and (b) Line 6. Least squares linear regression fits for samples collected at offshore stations (dashed) and at the three near shore stations (solid) are shown. The Anderson and Sarmiento (1994) $R_{(DIC/NO_3)}$ nutrient assimilation stoichiometry is also plotted (thick solid). Circles represent samples that were collected at offshore stations and squares represent the samples that were collected at the shelf break, mid-shelf, and near-shore stations.

away from shore while on Line 6 the ΔDIC_{CaCO_3} contribution was sporadic and ΔDIC_{Gas} decreased moving offshore. $\Delta DIC_{O.M.}$ was significantly larger than ΔDIC_{Gas} and ΔDIC_{CaCO_3} on both transects except at the near-shore stations. Near shore, gas exchange was more dominant in the DIC transformations than biological productivity and on Line 5 $CaCO_3$ dissolution played the largest role in the DIC transformation. The notable loss of DIC through gas evasion at the near-shore stations was likely driven by the large differences in pCO_2 between the sea surface and the atmosphere ($>$600 ppm). Larger ΔDIC_{Gas} values were observed on Line 6 than on Line 5 due to the longer timescales over which the mixed layers on Line 6 had been in contact with the atmosphere.

Residuals were large on both lines but were within or near the uncertainty limits at all stations on Line 6 and at the shelf break station on Line 5. Elevated residuals at the near-shore and mid-shelf stations on Line 5 may be due to the excess carbon over the continental shelf. If the water containing excess DIC relative to NO_3^- over the continental shelf was upwelled to the sea surface at the shoreline and advected offshore it could show up as residual DIC in the mixed layer analysis of the near shore stations. This source of carbon may also be responsible for the higher residuals in the mid-shelf and shelf break stations on Line 6, assuming advection transported the signal southward and offshore over time.

Another potential reason for the elevated mixed layer residuals on Line 5 may come from the use of a fixed DIC to NO_3^- assimilation ratio when determining $\Delta DIC_{O.M.}$. Biological productivity in upwelling regions is highly variable and nutrient assimilation ratios can vary widely depending on the maturity of a bloom, available nitrate, and available iron among other things (Dugdale et al., 2006; Franck et al., 2005; Hutchins and Bruland, 1998; Kudela and Dugdale, 2000; Kudela et al., 1997). After removing the $CaCO_3$ influence on ΔDIC ($\Delta DIC_{-TA}=\Delta DIC-\Delta DIC_{CaCO_3}$) and plotting ΔNO_3^- vs. ΔDIC_{-TA} for Line 5 (Fig. 5a) a transition in the slope of the trend line can be seen between the stations seaward of the shelf break and the stations over the shelf. A decrease in the ΔDIC_{-TA}:ΔNO_3^- ratio over the shelf means that the $\Delta DIC_{O.M.}$ values were likely overestimated in the mixed layer analyses for these stations, which could explain the "missing"

Table 4
Mixed layer ΔNO_3^-, $\Delta DIC_{O.M.}$ determined using the Anderson and Sarmiento (1994) C:N assimilation ratio, $\Delta DIC_{O.M.}$ determined using the slope of the ΔNO_3^- vs. ΔDIC_{-TA} trend line, the difference between the two $\Delta DIC_{O.M.}$ calculations, and the recalculated $\Delta DIC_{residual}$.

Line 5	ΔNO_3^- (μmol kg^{-1})	$\Delta DIC_{O.M.}$ A&S (μmol kg^{-1})	$\Delta DIC_{O.M.}$ Data (μmol kg^{-1})	$\Delta DIC_{O.M.(Data)} - \Delta DIC_{O.M.(A\&S)}$ (μmol kg^{-1})	$\Delta DIC_{residual}$ Data (μmol kg^{-1})
Near-shore	−0.2	−2	−1	1	11 ± 6
Mid-shelf	−3.9	−29	−22	7	4 ± 7
Shelf break	−2.2	−16	−12	4	−7 ± 6

source of ~11 μmol kg^{-1} DIC at the near-shore and mid-shelf stations on Line 5. On Line 6 the slope of the data trend (Fig. 5b) was slightly elevated in the near shore region, likely due to the extensive gas exchange near shore.

To estimate how large of an influence the fixed nutrient assimilation ratio had on the Line 5 DIC residuals, we used the ΔNO_3^- for each mixed layer and calculated the associated $\Delta DIC_{O.M.}$ using the slope of the ΔDIC_{-TA}:ΔNO_3^- trend line (5.5) for samples taken over the continental shelf (Table 4). Using the new $\Delta DIC_{O.M.}$ values, residuals were recalculated resulting in a significantly lower residual for the mid-shelf station but only a minimal reduction at the near-shore station (Table 4). As a result, fixed nutrient assimilation ratios could only account for some of the excess carbon in the Line 5 mixed layers. The remaining residual DIC at the near-shore station likely originated from the excess DIC overlying the sediments (~9 μmol kg^{-1}) as previously discussed.

Waters upwelling from reference depths of the near-shore, mid-shelf, and shelf break stations were undersaturated with respect to aragonite on both transects. By the time we sampled the mixed layers of these stations, ~0.22–4.1 days after the onset of upwelling, saturation had been restored at most stations due to a combination of biological productivity, gas exchange, and $CaCO_3$ dissolution. If these waters initially upwelled with the saturation states found at the reference or source water depths, surface waters over the entire continental shelf in the northern California region would have been undersaturated with respect to aragonite.

5.3. Projections of continued biological productivity in aged upwelled waters

During the occupation of Lines 5 and 6 a phytoplankton bloom was developing over the continental shelf but sampling concluded before all of the available nutrients had been utilized. By constructing a box model we estimate how continued primary productivity, until nutrient exhaustion, would have influenced the carbon characteristics of this water as it aged and was advected offshore. The model takes a Lagrangian approach, allowing gas exchange and biological productivity to occur simultaneously. Mixed layer depths were kept constant and the previously determined NCP rates were used to parameterize biological uptake of the remaining NO_3^- at the near-shore, mid-shelf, and shelf break stations.

Two simulations were also run for each station by applying the same box model used in the projection analysis, excluding the biological productivity component. The first of the two simulations involved instantaneously moving offshore, subsurface water to the surface and allowing gas exchange to occur. The second simulation involved moving water from just below the mixed layer to the surface and allowing gas exchange to occur (the same scenario as the projection analysis but without the biological activity). Both simulations used water from the same density surface found in the mixed layer at the station being evaluated. Differences between the two simulations for each station are due to the processes that occurred along the upwelling path.

Results for the projection and simulation runs for each station are shown in Fig. 6. By the time all remaining NO_3^- had been consumed in the projection analysis for each station, mixed layer DIC concentrations had been reduced by ~200 μmol kg^{-1} and sea surface pCO_2 levels were ~200 ppm, well below the atmospheric level. As a result of the drastic reductions in DIC and sea surface pCO_2, the aragonite saturation state (Ω_{Ar}) more than tripled at each station. The projections neglect further $CaCO_3$ dissolution so the increases in Ω_{Ar} were caused solely by reductions in DIC and increases in TA, which were driven by gas exchange and biological productivity.

Large differences in the evolution of pCO_2 and Ω_{Ar} over time between the simulations and the projection for each station are due to biological productivity. In the simulation runs only the near-shore stations on each line achieved $\Omega_{Ar} > 1.5$ and pCO_2 levels near the atmospheric concentration and these values were only reached due to the long simulation timescales for the near-shore stations. Timescales for the projection and simulation runs were determined by how quickly the remaining NO_3^- could be exhausted at the previously determined NCP rates for each station. On both lines, the near-shore station had the lowest NCP rate so it took significantly longer for biology to exhaust all available NO_3^- at these stations in the model. As a result of the longer timescales, more CO_2 was lost to the atmosphere leading to higher Ω_{Ar} values and lower pCO_2 values in the near-shore simulation runs. Due to these variable timescales the final Ω_{Ar} and pCO_2 levels reached in the simulations for a given station cannot be directly compared to those from other stations.

The timescales determined here, using fixed NCP rates to exhaust the remaining nutrients, are likely extreme overestimates. Nutrient assimilation rates, and thus NCP rates, generally increase over the course of bloom development, resulting in the complete exhaustion of nutrients in less than 10 days (Dugdale et al., 2006; MacIsaac and Dugdale 1969; Zimmerman et al., 1987). To test whether our simulation and projection results were significantly biased by the long timescales we performed a check by instantaneously removing all of the available nitrate that remained in the water at the time of measurement. To do this we took the nitrate concentration in the mixed layer at the time of measurement, converted it to units of DIC using $R_{(DIC/NO_3)}$ and then subtracted this from the measured DIC. We also corrected the TA for changes that occur as nitrate is consumed using $R_{(TA/NO_3)}$ and then re-equilibrated the carbonate system to determine the final carbon characteristics of the upwelled water. This calculation gave almost identical results to the model projection results at all stations (Table 5). The rapid biological uptake of DIC quickly reduced gas exchange rates in the projection analyses, and preformed nutrients in the water allowed the biology to draw the pCO_2 below the atmospheric level. Therefore, as the water aged it became a sink for atmospheric CO_2, counteracting the CO_2 efflux that occurred at the onset of upwelling when pCO_2 levels were high (~1000 ppm). As a result the net CO_2 exchange over the time period of nutrient assimilation was negligible.

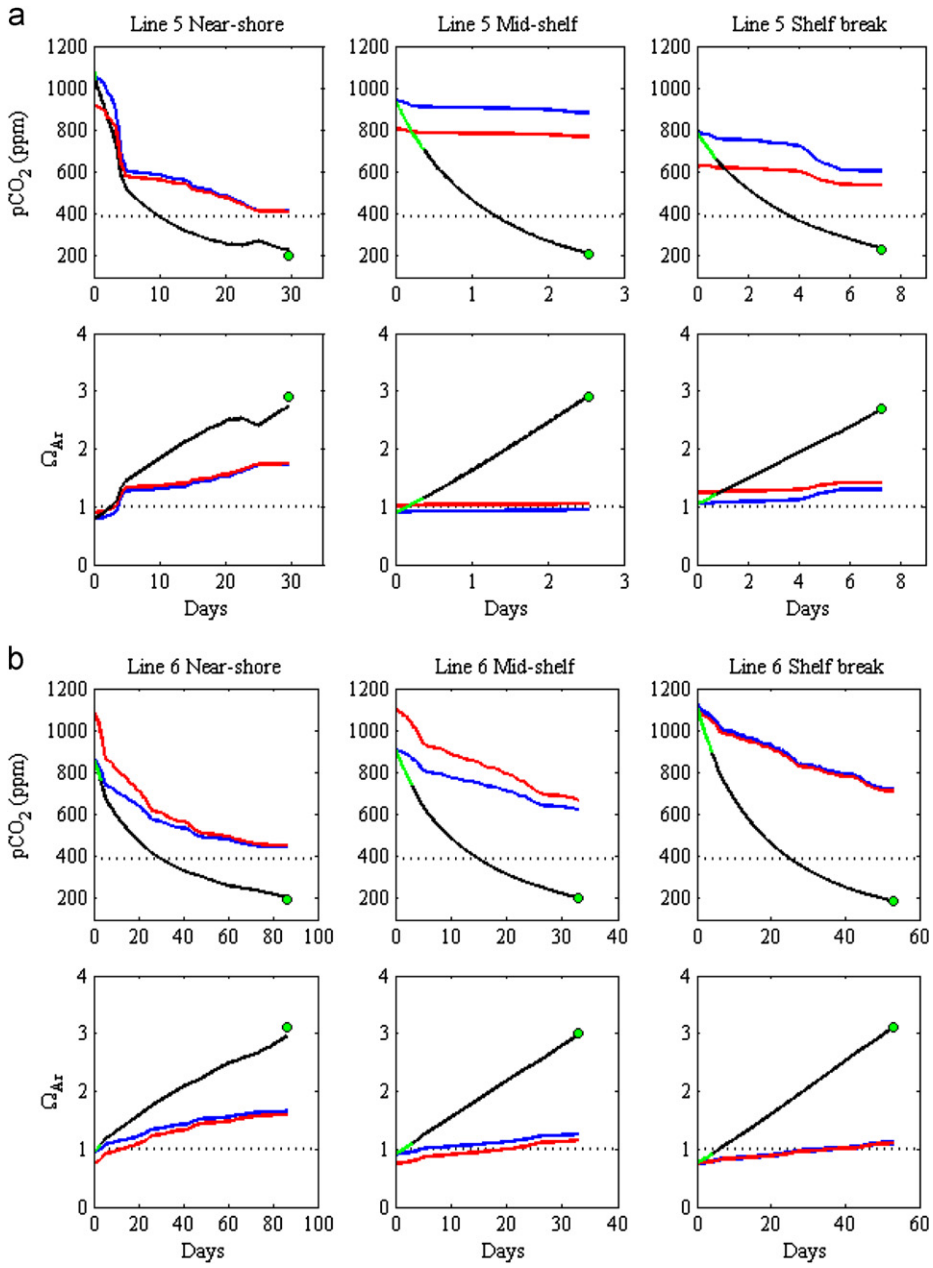

Fig. 6. pCO_2 (ppm) and Ω_{Ar} vs. time (day) for the projection and simulation analyses at the near-shore, mid-shelf, and shelf break stations on (a) Line 5 and (b) Line 6. Black lines show results of the projection analyses, blue lines show results of the simulation analyses that used water from below the mixed layer, and red lines show results of the simulation analyses that used offshore subsurface water. The short green lines at the beginning of each projection show what happened within the mixed layer from the time waters initially upwelled until the time of measurement. Green circles show the pCO_2 and Ω_{Ar} at each station after instantaneously removing the remaining available nitrate, leaving no time for gas exchange. (For interpretation of the references to color in this figure legend, the reader is referred to the web version of this article.)

6. Conclusions

The results of these analyses indicate that organic matter production and respiration had the largest influence on DIC transformations during each phase of the May 2007 upwelling event. The respiration of organic matter along the upwelling path caused waters to become undersaturated with respect to aragonite. This initiated the dissolution of $CaCO_3$ particles and resulted in a source of TA along the transit path. Over the continental shelf, where upwelling waters were outcropping, most surface waters had been returned to (super)saturated conditions by the time of measurement as a result of $CaCO_3$ dissolution, gas exchange, and biological productivity within the mixed layers. At the near-shore stations on each line, gas exchange and $CaCO_3$ dissolution played larger roles in the DIC transformations; however, at the mid-shelf and shelf break stations biological productivity dominated the DIC transformations (Table 6). By the time all of the available NO^{3-} had been consumed in the projection analyses sea surface pCO_2 values were well below atmospheric level ($\sim$200 ppm) and Ω_{Ar} were $\sim$3. In this analysis biological productivity rapidly reduced the ΔpCO_2 between the sea surface and the atmosphere until pCO_2 levels fell well below the atmospheric concentration. As a result, the net gas exchange in the forward projections was found to be negligible, indicating that the transition of coastal

Table 5
Mixed layer pCO_2 (μatm), Ω_{Ar}, DIC (μmol kg^{-1}), TA (μmol kg^{-1}), NO_3^- (μmol kg^{-1}), and Ω_{Ca} at the time of measurement (ML), at the end of the projection analysis (Proj.), and after instantaneously removing the remaining available NO_3^- (Inst.).

	Near-shore			Mid-shelf			Shelf break		
	ML	**Proj.**	**Inst.**	**ML**	**Proj.**	**Inst.**	**ML**	**Proj.**	**Inst.**
Line 5									
pCO_2	1004	228	205	699	211	211	656	237	233
Ω_{Ar}	0.8	2.7	2.9	1.2	2.9	2.9	1.2	2.7	2.7
DIC	2226	2024	2003	2174	2000	2000	2130	1988	1984
TA	2263	2286	2286	2259	2280	2280	2223	2243	2243
NO_3^-	30	0	0	24	0	0	20	0	0
Ω_{Ca}	1.3	4.3	4.6	1.8	4.6	4.6	1.9	4.2	4.3
Line 6									
pCO_2	738	204	195	735	204	204	875	188	189
Ω_{Ar}	1.1	3.0	3.1	1.1	3.0	3.0	0.9	3.1	3.1
DIC	2200	2012	2003	2194	2012	2012	2221	2001	2002
TA	2277	2297	2297	2271	2297	2297	2275	2302	2302
NO_3^-	27	0	0	25	0	0	30	0	0
Ω_{Ca}	1.7	4.7	4.8	1.7	4.7	4.7	1.5	4.9	4.9

Table 6
$\Delta DIC_{O.M.}$, ΔDIC_{CaCO_3}, ΔDIC_{Gas}, and $\Delta DIC_{residual}$ expressed as percentages of the total ΔDIC. The largest percentages for each station are highlighted in bold.

	Line 5			Line 6		
	Near-shore	**Mid-shelf**	**Shelf break**	**Near-shore**	**Mid-shelf**	**Shelf break**
$\%\Delta DIC_{O.M.}$	8	**63**	**70**	34	**57**	**45**
$\%\Delta DIC_{CaCO_3}$	23	4	2	18	0	7
$\%\Delta DIC_{Gas}$	12	8	15	**44**	19	21
$\%\Delta DIC_{residual}$	**57**	25	13	5	24	27

upwelled waters from near shore sources to offshore sinks for atmospheric CO_2 is largely controlled by the rapid biological reduction of DIC in upwelled waters.

The aragonite saturation horizon in the North Pacific Ocean is the shallowest in the world ocean and is shoaling as the oceans continue to absorb anthropogenic CO_2 from the atmosphere (Feely et al., 2004). Ocean–carbon cycle models that do not include coastal upwelling indicate that the sea surface will not be undersaturated with respect to aragonite until ~2100 (Orr et al., 2005); however, Feely et al. (2004) have shown that coastal upwelling in the CCS is already exposing planktonic communities in the northern California region to waters that are undersaturated with respect to aragonite. The most recent review articles concerning the biological responses of calcifying marine organisms to ocean acidification indicate that a vast majority of organisms are adversely affected when exposed to undersaturated waters (Doney et al., 2009; Fabry et al., 2008; Guinotte and Fabry, 2008). Many of these studies have focused on infaunal adult organisms; however, the early life states of some calcifying species involve planktonic larval stages that may be more sensitive (Todgham and Hofmann 2009; O'Donnel et al., 2009; Green et al., 2004). Recent work on larvae of the purple sea urchin *Strongylocentrotus purpuratus*, a benthic invertebrate found in coastal ecosystems along the west coast of North America, has shown that low pH and high pCO_2 conditions cause physiological changes in the larvae, which reduce their ability to tolerate environmental stress (Todgham and Hofmann 2009; O'Donnel et al., 2009). These findings suggest the adaptability of some coastal marine species to ocean acidification may be dependent on larval resilience in regions where undersaturated waters upwell to the sea surface.

Our observations indicate that a natural, respiration derived, acidification of at least ~35 μmol kg^{-1} DIC can occur in the waters that upwell along the coast of northern California. These waters currently hold ~31 μmol kg^{-1} of anthropogenic DIC (Feely et al., 2008), indicating that humans may have already doubled the acidification of these waters relative to preindustrial times. Currently, primary producers are modifying the carbon characteristics of the upwelled waters at a rate that significantly reduces the stress of aragonite undersaturation over the course of a few days. In the future, when these upwelled waters contain even more anthropogenic CO_2, more biological productivity will be required in order to achieve low enough pCO_2 levels for aragonite to be saturated. Because the CO_2 reduction of upwelled water is primarily biologically controlled there is potential that it will also be sensitive to increasing pCO_2 levels and decreasing Ω_{Ar} and/or Ω_{Ca}. Further research is necessary to determine how this mechanism will change in the future as the oceans continue to absorb anthropogenic CO_2 and saturation horizons continue to shoal.

Acknowledgments

The authors would like to thank Captain Richard Verlini and the crew of the *R/V Wecoma* for their assistance at sea and the members of the Feely/Sabine/Allen lab at PMEL, who were involved in the *NACP West Coast Cruise*. Special thanks to Burke Hales (Oregon State University) for his support and to Julia Hummon (University of Hawaii) who provided ADCP data used in this analysis. This study benefited from discussions with Laurie Juranek (NOAA/PMEL), Steve Emerson (University of Washington), and Barbara Hickey (University of Washington). Financial support for this work was provided by the National Oceanic and Atmospheric Administration's Global Carbon cycle Program and the National Aeronautical and Space Administration Ocean Biology and Biogeochemistry Program. This publication is partially funded by the University of Washington Graduate School and Program on Climate Change, as well as the Joint Institute for the Study of the Atmosphere and Ocean (JISAO) under NOAA Cooperative Agreement no. NA17RJ1232. This research is contribution 3550 to NOAA's Pacific Marine Environmental Laboratory, and contribution 1819 to JISAO.

Appendix

Error analysis

Standard error propagation methods were used to propagate uncertainties in the sample measurements and in the Anderson and Sarmiento (1994) nutrient assimilation ratios ($P/N/C_{org}/O_2 = 1/16 \pm 1/117 \pm 14/170 \pm 10$). NDBC (http://www.ndbc.noaa.gov/) ARES Payload accuracy guidelines (http://www.ndbc.noaa.gov/rsa.shtml) were used to determine the uncertainty in winds from NDBC buoys 46027 and 46022 (Fig. 1a). Wind errors were propagated through piston velocity calculations (Nightingale et al., 2000) resulting in piston velocity errors ranging from 20% to 40%. The median error (~25%) was selected for further error propagation.

Relative errors in the piston velocity (25%) and mixed layer depth (20%) were used to determine the relative error ($(0.2^2+0.25^2)^{0.5} \sim 0.32$) in the cumulative oxygen gas exchange for each time step in the mixed layer oxygen model. Because these relative errors were fixed, for each time step in the model there

was a 32% uncertainty in the total amount of oxygen gained from gas exchange. Uncertainty in the $([O_2]_h - [O_2]_{sat})$ term was negligible compared to the other uncertainties in the gas exchange calculation, and was therefore omitted from the error analysis. Uncertainty in the cumulative biological productivity term was determined using the relative errors in ΔNO_3^-, $R_{(O_2/No_3)}$, and in the mixed layer depth. The cumulative gas exchange and the biological productivity term uncertainties were then combined with the oxygen measurement uncertainty (± 0.2 μmol kg^{-1}) to calculate a total uncertainty (*) in $[O_2]_{h(t=n+1)}$ for each time step in the oxygen model:

$$^*[O_2]_{h(t=n+1)} = \left(^*[O_2]^2_{h(\text{meas.})} + {}^*\Delta O2^2_{2\text{Gas}(t=n)} + {}^*\Delta O2^2_{2\text{O.M.}(t=n)}\right)^{0.5} \quad \text{(A1)}$$

Mixed layer ages were determined when $[O_2]_h$ equaled $[O_2]_{\text{reference}}$. This solution was almost explicit due to the small time step in the model; however, due to uncertainties in the calculated $[O_2]_h$ for each time step, as well as the uncertainty in the offshore $[O_2]_{\text{reference}}$ measurement (± 0.2 μmol kg^{-1}), the range of possible mixed layer residence times was much larger than the time step limitations. Uncertainty in the mixed layer age depended on the first and last time steps during which the error bars for the calculated $[O_2]_h$ were within the uncertainty limits of $[O_2]_{\text{reference}}$. The difference between these and the time step at which $[O_2]_h$ equaled $[O_2]_{\text{reference}}$ gave the error bars for Δt. The mean of these error bars was propagated with the uncertainty in $\Delta DIC_{O.M.}$ to derive an uncertainty in the NCP rate ($NCP = \Delta DIC_{O.M.}/\Delta t$).

Similarly, in the CO_2 gas exchange model uncertainties in the cumulative gas exchange, biological, and calcite dissolution terms were calculated for each time step and propagated with the DIC measurement error (± 1.5 μmol kg^{-1}) to get a total error in the calculated mixed layer DIC_h (Eq. (A2)). The same approach was taken to calculate the error in TA_h for each time step (Eq. (A3)). At the end of the model run, errors in TA_h and DIC_h ($\sim$4 and $\sim$3 μmol kg^{-1}, respectively) were used to determine how sensitive the pCO_2 calculation was to uncertainties in these input parameters. Uncertainty in the input parameters resulted in a 2.5% uncertainty in the calculated pCO_2, which was insignificant relative to errors in the piston velocity and the mixed layer depth:

$$^*DIC_{h(t=n+1)} = \left(^*DIC^2{}_{(\text{meas.})} + {}^*\Delta DIC^2{}_{\text{Gas}(t=n)} + {}^*\Delta DIC^2{}_{\text{O.M.}(t=n)} + {}^*\Delta DIC^2{}_{\text{CaCO}_3(t=n)}\right)^{0.5} \quad \text{(A2)}$$

$$^*TA_{h(t=n+1)} = \left(^*TA^2{}_{(\text{meas.})} + {}^*\Delta TA^2{}_{\text{O.M.}(t=n)} + {}^*\Delta TA^2{}_{\text{CaCO}_3(t=n)}\right)^{0.5} \quad \text{(A3)}$$

Summing the gas exchange terms from each time step over the age of the mixed layer gave the total DIC loss due to gas exchange. The calculation was also completed using the upper and lower mixed layer age uncertainty limits, giving a range of uncertainty in ΔDIC_{Gas}. The mean of the ΔDIC_{Gas} error bars was propagated to determine the uncertainty in $\Delta DIC_{residual}$.

References

Allen, J.S., Newberger, P.A., Federiuk, J., 1995. Upwelling circulation on the Oregon continental-shelf .1. Response to idealized forcing. J. Phys. Oceanogr. 25, 1843–1866.

Anderson, L.A., Sarmiento, J.L., 1994. Redfield ratios of remineralization determined by nutrient data analysis. Global Biogeochem. Cycles 8, 65–80.

Carpenter, J.H., 1965. The Chesapeake Bay Institute technique for the Winkler dissolved oxygen method. Limnol. Oceanogr. 10, 141–143.

Chavez, F.P., Barber, R.T., Kosro, P.M., Huyer, A., Ramp, S.R., Stanton, T.P., De Menodal, B.R., 1991. Horizontal transport and the distribution of nutrients in the coastal transition zone off northern California; effects on primary production, phytoplankton biomass and species composition. J. Geophys. Res. 96, 14,833–14,848.

Chavez, F.P., Toggweiler, J.R., 1995. Physical estimates of global new production: the upwelling contribution. In: Summerhayes, C.P., Emeis, K.C., Angel, M.V., Smith, R.L., Zeitzschel, B. (Eds.), Upwelling in the Ocean: Modern Processes and Ancient Records. J. Wiley & Sons, Inc., Chichester, pp. 313–320.

Culberson, C.H., Knapp, G., 1991. A Comparison of Methods for the Determination of Dissolved Oxygen in Seawater. Report WHPO 91-2. WOCE Hydrographic Program Office.

Dickson, A.G., Afghan, J.D., Anderson, G.C., 2003. Reference materials for oceanic CO_2 analysis: a method for the certification of total alkalinity. Mar. Chem. 80, 185–197.

Dickson, A.G., Millero, F.J., 1987. A comparison of the equilibrium-constants for the dissociation of carbonic-acid in seawater media. Deep Sea Res. A 34, 1733–1743.

Doney, S.C., Fabry, V.J., Feely, R.A., Kleypas, J.A., 2009. Ocean acidification: the other CO_2 problem. J. Mar. Res. 1, 169–192.

Dugdale, R.C., Wilkerson, F.P., Hogue, V.E., Marchi, A., 2006. Nutrient controls on new production in the Bodega Bay, California, coastal upwelling plume. Deep Sea Res. Pt. II: Top. Stud. Oceanogr. 53, 3049–3062.

Fabry, V.J., Seibel, B.A., Feely, R.A., Orr, J.C., 2008. Impacts of ocean acidification on marine fauna and ecosystem processes. J. Mar. Res. 65, 414–432.

Feely, R.A., Sabine, C.L., Hernandez-Ayon, J.M., Ianson, D., Hales, B., 2008. Evidence for upwelling of corrosive "acidified" water onto the continental shelf. Science 320, 1490–1492.

Feely, R.A., Sabine, C.L., Lee, K., berelson, W., Kleypas, J., Fabry, V.J., Millero, F.J., 2004. Impact of anthropogenic CO_2 on the $CaCO_3$ system in the oceans. Science 305, 362–366.

Franck, V.M., Smith, G.J., Bruland, K.W., Brzezinski, M.A., 2005. Comparison of size-dependent carbon, nitrate, and silicic acid uptake rates in high- and low-iron waters. Limnol. Oceanogr. 50, 825–838.

Garcia, H.E., Gordon, L.I., 1992. Oxygen solubility in seawater: better fitting equations. Limnol. Oceanogr. 37, 1307–1312.

Gordon, L.I., Jennings Jr., J.C., Ross, A.A., Krest, J.M., 1992. A Suggested Protocol for Continuous Flow Automated Analysis of Seawater Nutrients (Phosphate, Nitrate, Nitrite and Silicic Acid) in the WOCE Hydrographic Program and the Joint Global Ocean Fluxes Study. WOCE Hydrographic Program Office Methods Manual WHPO 91-1.

Green, M.A., Jones, M.E., Boudreau, C.L., Moore, R.L., Westman, B.A., 2004. Dissolution mortality of juvenile bivalves in coastal marine deposits. Limnol. Oceanogr. 49, 727–734.

Guinotte, J.M., Fabry, V.J., 2008. Ocean acidification and its potential effects on marine ecosystems. Ann. N.Y. Acad. Sci. 1134, 320–342.

Hales, B., Moum, J.N., Covert, P., Perlin, A., 2005a. Irreversible nitrate fluxes due to turbulent mixing in a coastal upwelling system. J. Geophys. Res., 110. doi:10.1029/2004JC002685.

Hales, B., Takahashi, T., Bandstra, L., 2005b. Atmospheric CO_2 uptake by a coastal upwelling system. Global Biogeochem. Cycles, 19. doi:10.1029/2004GB002295.

Hickey, B.M., 1979. The California Current System: hypotheses and facts. Prog. Oceanogr. 8, 191–279.

Hickey, B.M., 1998. Coastal oceanography of Western North America from the tip of Baja California to Vancouver Island. In: Brink, K.H., Robinson, A.R. (Eds.), The Sea. J. Wiley and Sons, Inc., New York, pp. 345–393.

Hickey, B.M., Banas, N.S., 2008. Why is the northern end of the California current system so productive? Oceanography 21, 90–107.

Hutchins, D.A., Bruland, K.W., 1998. Iron-limited diatom growth and Si:N uptake ratios in a coastal upwelling regime. Nature 393, 561–564.

Huyer, A., 1983. Coastal upwelling in the California Current System. Prog. Oceanogr. 12, 259–284.

Huyer, A., Sobey, E.J.C., Smith, R.L., 1979. Spring transition in currents over the Oregon continental-shelf. J. Geophys. Res. 84, 6995–7011.

Ianson, D., Allen, S.E., Harris, S.L., Orians, K.J., Varela, D.E., Wong, C.S, 2003. The inorganic carbon system in the coastal upwelling region west of Vancouver Island, Canada. Deep Sea Res. Pt. I Oceanogr. Res. Pap. 50, 1023–1042.

Jahne, B., Heinz, G., Dietrich, W., 1987. Measurement of the diffusion coefficients of sparingly soluble gases in water. J. Geophys. Res. 92, 10,767–10,776.

Jiang, L., Cai, W., Wanninkhof, R., Wang, Y., Luger, H., 2008. Air–sea CO_2 fluxes on the U.S. South Atlantic Bight: spatial and seasonal variability. J. Geophys. Res., 113. doi:10.1029/2007JC004366.

Johnson, K.M., 1992. Operator's Manual: Single-operator Multiparameter Metabolic Analyzer (SOMMA) for Total Carbon Dioxide (CT) with Coulometric Detection. Brookhaven National Laboratory, Brookhaven, NY 70 pp.

Johnson, K.M., King, A.E., Sieburth, J.M., 1985. Coulometric DIC analyses for marine studies: an introduction. Mar. Chem. 16, 61–82.

Johnson, K.M., Sieburth, J.M., Williams, P.J.LeB, Brandstrom, L., 1987. Coulometric total carbon-dioxide analysis for marine studies: automation and calibration. Mar. Chem. 21, 117–133.

Johnson, K.M., Wills, K.D., Butler, D.B., Johnson, W.K., Wong, C.S., 1993. Coulometric total carbon-dioxide analysis for marine studies: maximizing the performance of an automated gas extraction system and coulometric detector. Mar. Chem. 44, 167–187.

Kudela, R.M., Cochlan, W.P., Dugdale, R.C., 1997. Carbon and nitrogen uptake response to light by phytoplankton during an upwelling event. J. Plankton Res. 19, 609–630.

Kudela, R.M., Dugdale, R.C., 2000. Nutrient regulation of phytoplankton productivity in Monterey Bay, California. Deep Sea Res. Pt. II Top. Stud. Oceanogr. 47, 1023–1053.

Lentz, S.J., 1992. The surface boundary layer in coastal upwelling regions. J. Phys. Oceanogr. 22, 1517–1539.

Lewis, E., Wallace, D.W.R., 1998. Program Developed for CO_2 System Calculations. ORNL/CDIAC-105. Carbon Dioxide Information Analysis Center, Oak Ridge National Laboratory, U.S. Department of Energy, Oak Ridge, Tennessee.

MacIsaac, J.J., Dugdale, R.C., Barber, R.T., Blasco, D., Packard, T.T., 1985. Primary production cycle in an upwelling center. Deep Sea Res. A 32, 503–529.

MacIsaac, J.J., Dugdale, R.C., 1969. Kinetics of nitrate and ammonia uptake by natural populations of marine phytoplankton. Deep Sea Res. A 16, 45–57.

Mehrbach, C., Culberson, C.H., Hawley, J.E., Pytkowic, R.M., 1973. Measurement of apparent dissociation-constants of carbonic-acid in seawater at atmospheric-pressure. Limnol. Oceanogr. 18, 897–907.

Nightingale, P.D., Malin, G., Law, C.S., Watson, A.J., Liss, P.S., Liddicoat, M.I., Boutin, J., Upstill-Goddard, R.C., 2000. In situ evaluation of air–sea gas exchange parameterizations using novel conservative and volatile tracers. Global Biogeochem. Cycles 14, 373–387.

O'Donnel, M.J., Hammond, L.M., Hofmann, G.E., 2009. Predicted impact of ocean acidification on a marine invertebrate: elevated CO_2 alters response to thermal stress in sea urchin larvae. Mar. Biol. 156, 439–446.

Orr, J.C., Fabry, V.J., Aumont, O., Bopp, L., Doney, S.C., Felly, R.A., Gnanadesikan, A., Gruber, N., Ishida, A., et al., 2005. Anthropogenic ocean acidification over the twenty-first century and its impact on calcifying organisms. Nature 437, 681–686.

Pilskaln, C.H., Paduan, J.B., Chavez, F.P., Anderson, R.Y., Berelson, W.M., 1996. Carbon export and regeneration in the coastal upwelling system of Monterey Bay, central California. J. Mar. Res. 54, 1149–1178.

Redfield, A.C., et al., 1963. The influence of organisms on the composition of seawater. In: Hill, M.N. (Ed.), The Sea: Ideas and Observations on Progress in the Study of the Seas, vol. 2. John Wiley, Hoboken, NJ, pp. 26–77.

Strub, P.T., Allen, J.S., Huyer, A., Smith, R.L., 1987a. Large-scale structure of the spring transition in the coastal ocean off western North America. J. Geophys. Res. 92, 1527–1544.

Strub, P.T., Allen, J.S., Huyer, A., Smith, R.L., 1987b. Seasonal cycle of currents, temperatures, winds, and sea level over the northeast Pacific continental shelf: 35°N to 48°N. J. Geophys. Res. 92, 1507–1526.

Sweeney, C., Gloor, E., Jacobson, A.R., Key, R.M., McKinley, G., Sarmineto, J.L., Wanninkhof, R., 2007. Constraining global air–sea gas exchange for CO_2 with recent bomb ^{14}C measurements. Global Biogeochem. Cycles, 21. doi:10.1029/2006GB002784.

Todgham, A.E., Hofmann, G.E., 2009. Transcriptomic response of sea urchin larvae *Strongylocentrotus pupuratus* to CO_2-driven seawater acidification. J. Exp. Biol. 212, 2579–2594.

van Geen, A., Takesue, R.K., Goddard, J., Takahashi, T., Barth, J.A., Smith, R.L., 2000. Carbon and nutrient dynamics during coastal upwelling off Cape Blanco, Oregon. Deep Sea Res. Pt. II Top. Stud. Oceanogr. 47, 975–1002.

Wanninkhof, R., 1992. Relationship between wind speed and gas exchange over the ocean. J. Geophys. Res. 97, 7373–7382.

Wanninkhof, R., Asher, W.E., Ho, D.T., Sweeney, C., McGillis, W.R., 2009. Advances in quantifying air–sea gas exchange and environmental forcing. Annu. Rev. Mar. Sci. 1, 213–244.

Weiss, R.F., 1974. Carbon dioxide in water and seawater: the solubility of a non-ideal gas. Mar. Chem. 2, 203–215.

Wetz, M.S., Hales, B., Wheeler, P.A., 2008. Degradation of phytoplankton-derived organic matter; implications for carbon and nitrogen biogeochemistry in coastal ecosystem. Estuar. Coast. Shelf Sci. 77, 422–432.

Wilke, R.J., Wallace, D.W.R., Johnson, K.M., 1993. Water-based gravimetric method for the determination of gas loop volume. Anal. Chem. 65, 2403–2406.

Wise, D.L., Houghton, G., 1966. The diffusion coefficients of ten slightly soluble gases in water at 10–60 °C. Chem. Eng. Sci. 21, 999–1010.

Zimmerman, R.C., Kremer, J.N., Dugdale, R.C., 1987. Acceleration of nutrient uptake by phytoplankton in a coastal upwelling ecosystem: a modeling analysis. Limnol. Oceanogr. 32, 359–367.